



Structure-based identification of potent VEGFR-2 inhibitors from in vivo metabolites of a herbal ingredient

Raju Dash^{1,2,3} · Md. Junaid¹ · Sarmistha Mitra⁴ · Md Arifuzzaman^{3,5} · S. M. Zahid Hosen¹

Received: 30 October 2017 / Accepted: 5 March 2019 / Published online: 23 March 2019
© Springer-Verlag GmbH Germany, part of Springer Nature 2019

Abstract

Vascular endothelial growth factor receptor-2 (VEGFR-2) is one of the regulatory elements of angiogenesis that is expressed highly in various diseases and is also essential for solid tumor growth. The present study was aimed at identifying potent inhibitors of VEGFR-2 by considering herbal secondary metabolites; as natural molecules are less toxic than synthetic derivatives. A structure-based virtual screening protocol consisting of molecular docking, MM-GBSA and ADME/T analysis was initially used to screen a library of in vivo metabolites of the herbal ingredient. Using a fixed cutoff value, four potent virtual hits were identified from molecular docking, ADME/T and binding affinity calculations, which were considered further for molecular dynamics (MD) simulation to broadly describe the binding mechanisms to VEGFR-2. The results suggested that these molecules have high affinity for the catalytic region of VEGFR-2, and form strong hydrophobic and polar interactions with the amino acids involved in the binding site of ATP and linker regions of the catalytic site. Subsequently, the stability of the docked complexes and binding mechanisms were evaluated by MD simulations, and the energy of binding was calculated through MM-PBSA analysis. The results uncovered two virtual hits, designated **ZINC14762520** and **ZINC36470466**, as VEGFR-2 inhibitors, and suggested that they bind to kinase domain in an ATP-competitive manner. These virtual hits will offer a suitable starting point for the further design of their various analogs, allowing a rational search for more effective inhibitors in the future.

Keywords VEGFR-2 · Angiogenesis · Molecular docking · Molecular dynamics · MM-PBSA

Abbreviations

ADME/T	Absorption distribution metabolism excretion and toxicity	MD	Molecular dynamics
AMBER	Assisted model building with energy refinement	MM	Molecular mechanics
HTVS	High throughput virtual screening	MM-GBSA	Molecular mechanics - generalized born and surface area
KDR	Kinase insert domain receptor	OPLS	Optimized potential for liquid simulations
		PBSA	Poisson–Boltzmann surface area

Electronic supplementary material The online version of this article (<https://doi.org/10.1007/s00894-019-3979-6>) contains supplementary material, which is available to authorized users.

✉ S. M. Zahid Hosen
smzahidhosen@bcsir.gov.bd

Raju Dash
rajudash.bgctub@gmail.com

Md. Junaid
md.junaid@northsouth.edu

Sarmistha Mitra
sarmisthacu@gmail.com

Md Arifuzzaman
larif67@yahoo.com

¹ Molecular Modeling and Drug Design Laboratory, Pharmacology Research Division, Bangladesh Council of Scientific and Industrial Research (BCSIR), Chittagong 4220, Bangladesh

² Department of Anatomy, Dongguk University Graduate School of Medicine, Gyeongju 38066, Republic of Korea

³ Department of Biochemistry and Biotechnology, University of Science and Technology Chittagong, Chittagong 4202, Bangladesh

⁴ Plasma Bioscience Research Center, Plasma-bio display, Kwangwoon University, Seoul 01897, Republic of Korea

⁵ Department of Natural Sciences, LAGCC, City University of New York (CUNY), New York, NY, USA

PME	Particle mesh Ewald
Rg	Radius of gyration
RMSD	Root mean square deviation
RMSF	Root mean square fluctuation
SAR	Structure activity relationship
SASA	Solvent accessible surface area
SGB	Surface generalized Born
SP	Standard precision
TIP3P	The transferable intermolecular potential3 points
VEGFR-2	Vascular endothelial growth factor receptor 2
XP	Extra precision
YASARA	Yet another scientific artificial reality application

Introduction

The process by which new blood vessel is formed—dubbed Angiogenesis—has recently gained significant attention in anticancer drug development. The process of angiogenesis is pivotal in solid tumor growth, diabetes and other age-related diseases [1, 2]. In solid tumor, blood vessels are formed excessively to confer sufficient oxygen and nutrient supply to malignant cells in order to establish the process of metastasis [3]. Evidence has also shown that vascular endothelial growth factor (VEGF) and its receptors (VEGFRs) are the main modulators of angiogenesis [4, 5].

The members of VEGFR including VEGFRs 1–3 are targeted by VEGF, which binds to the extracellular domain of VEGFRs to activate downstream signaling pathways [3]. VEGFR-2 (KDR) directly regulates endothelial cell proliferation and migration [6–8]. Upon binding of VEGF-A, the tyrosine residues at the carboxy-terminal of the receptor are autophosphorylated, thus activating cell signaling, vasculogenesis, and angiogenesis [9, 10]. Aggressive expression of VEGFR-2 activates downstream pathways of cell survival, which makes this an attractive target for developing novel anticancer agents.

A number of VEGFR inhibitors are currently in phase I or phase II clinical trials [11], while other inhibitors, such as sorafenib (Nexavar®, BAY 43–9006), sunitinib malate (Sutent®, SU11248), and bevacizumab (Avastin®), are already approved for cancer treatment by the Food and Drug Administration (FDA) [12]. Pharmacologically, they act by blocking the VEGFR pathway; however, their prolonged use can lead to serious side-effects, such as bleeding, gastrointestinal perforation and hypertension [13, 14]. Therefore, the search for novel and potent VEGFR inhibitors that could effectively block angiogenesis remains a major challenge in anti-angiogenic drug development.

Due to their high efficacy and lower toxicity, compounds from natural sources have recently gained more attention as anti-angiogenesis agents [15]. Nevertheless, they still suffer from poor bioavailability [16]. Consequently, in vivo metabolites of some herbal compounds were found to show better pharmacokinetic, potency and safety profiles in comparison to their parent compounds [17]. For this reason, to find potent VEGFR-2 inhibitors with optimum pharmacokinetic profiles, this study applied a virtual in silico screening approach using a database of in vivo metabolites of herbal ingredients. The virtual screening procedure was integrated with a three-step filtering approach, including Glide XP docking, ADME/T and MM-GBSA analysis, to sort out the top hits from the database (Fig. S1, see Supplementary file 1). After that, each docked protein–ligand complex was subjected to 100-ns MD simulations along with binding energy calculations through MM-PBSA analysis, in order to elucidate the VEGFR-2 binding mechanisms of identified compounds. The study identified two virtual hits, **ZINC14762520** and **ZINC36470466**, that could be potent VEGFR-2 inhibitors, and also suggested a basis for further rational design of their various analogs to find more effective inhibitors in the future.

Materials and methods

Database processing

A dataset of in vivo secondary metabolites of herbal ingredients was retrieved from the ZINC server named Herbal Ingredients In-Vivo Metabolism (HIM) (last updated: 12 August 2013), giving a set of 663 in-vivo metabolites of herbal active ingredients. Although the ZINC database consists of molecules ready to dock in three dimensional (3D) formats, to make it more rationale, we further prepared the dataset using Schrödinger Suite 2013 [18, 19] software. Here, all ligands were minimized in Ligprep2.5 wizard [20], by implementing OPLS 2005 [21] force field. During the minimization, the module Epik 2.2 [22] was utilized to fix the ionization state of the ligand at pH 7.0 ± 2.0 [23]. From this analysis, up to 32 possible stereoisomers of each compound were generated; we selected only the conformer having the lowest energy for further processing.

Protein preparation and grid generation

Protein structures for virtual screening were prepared using the protein preparation module of Schrödinger Suite 2013 [19] software, in which the crystal structure is initially assigned proper hydrogen, charges and bond orders. As the main target of the virtual screening was VEGFR-2, its tyrosine kinase domain was retrieved from the RCSB protein data bank (PDB id: **3B8R**) [24]. At neutral pH, all hydrogen bonds in the

structure were optimized, deleting unnecessary water. Afterwards, the minimization process was run with the OPLS 2005 force field, considering structural changes of not more than 0.30 Å of RMSD. The active site of the protein was fixed for docking simulation by generating a grid box at the reference ligand binding the protein. Grid generation parameters were kept at default, with a box size of 18 Å × 18 Å × 18 Å, and the OPLS 2005 force field utilized for post minimization. The charge cutoff and van der Waals scaling factor were set to 0.25 and 1.00, respectively [25].

Virtual screening

We carried out extra precision (XP) flexible docking using the Glide module of Schrödinger-Maestro v9.4 [26, 27], which is more sophisticated than SP/HTVS in scoring function [27]. Here, all ligands were treated flexibly, considering the partial charge and van der Waals factor of 0.15 and 0.80, respectively. Minimization was performed to the docked complex after docking using the OPLS 2005 force field. The best-docked pose with lowest Glide score value was recorded for each ligand [25].

ADME/T analysis

In order to predict the pharmacokinetic profile of the identified hits, QikProp (Schrodinger Suite 2013) [28] was utilized, where the absorption, distribution and metabolism of each ligand were calculated. Pharmacokinetics and the drug-like properties of the ligands, such as the rate of oral absorption, QlogP, solvent accessible surface area (SASA), and Lipinski's rule of five [29], were predicted, and maximum percentage of oral absorption rate with a cutoff of 50% was considered for selecting the top hits for further processing.

Prime MM-GBSA

Binding affinity calculations were carried out using the Prime MM-GBSA module of the Schrodinger suite [30], where greater negative affinity denotes higher stability. The docked Pose viewer file from Glide XP docking was introduced for calculation, using the sampling minimization protocol used Generalized Born Surface Accessible (GBSA) as a continuum model, and OPLS 2005 force field as molecular mechanics (MM), keeping the protein flexible [31–35]. For correcting empirical functions of π -stacking and H-bond interactions, a dielectric solvent model such as VSGB 2.0 [36] was used.

MD simulations

MD simulations were performed using YASARA Dynamics software [37], and the AMBER14 force field [38]. A total of six different systems were used to run MD simulation. The

systems included top four virtual hits, (ZINC13370550-VEGFR-2, ZINC02585769-VEGFR-2, ZINC14762520-VEGFR-2 and ZINC36470466-VEGFR-2 complexes), sunitinib-VEGFR-2, and apo-VEGFR-2. In each protein–ligand complex, the parameters of each ligand were assigned through AutoSMILES [39] algorithms, where unknown organic molecules are parameterized fully automatically by the calculation of semi-empirical AM1 Mulliken point charges [39] with the COSMO solvation model, assigning of AM1BCC [40] atom and bond types, and also assigning GAFF [41] (General AMBER Force Field) atom types and the remaining force field parameters. Before simulation, the hydrogen bonding network of the protein–ligand complex was optimized and solvated by a TIP3P [42] water model in a simulation cell. Periodic boundary conditions were maintained with a solvent density of 0.997 gL⁻¹. Titratable amino acids in the protein complex were subjected to pKa calculation during solvation. The initial energy minimization process of each simulation system, consisting of 62,521 ± 10 atoms was performed by a simulated annealing method, using the steepest gradient approach (5000 cycles). Each simulation was run with a multiple time step algorithm [43], using a time-step interval of 2.50 fs under physiological conditions (298 K, pH 7.4, 0.9% NaCl) [44]. All bond lengths were constrained using the linear constraint solver (LINCS) [45] algorithm, and SETTLE [46] was used for water molecules. Long-range electrostatic interactions were described by the PME [47] methods, and, finally, 100 ns MD simulation was accomplished at Berendsen thermostat [48] and constant pressure. For further analysis, the trajectories were saved every 250 ps, and subsequent analysis was performed by default script of YASARA [49] macro and VMD [50, 51] software.

All snapshots were further subjected to MM-PBSA (MM-Poisson–Boltzmann surface area) binding free energy calculation by YASARA software using the following formula [52],

$$\text{Binding Energy} = E_{\text{potRecept}} + E_{\text{solvRecept}} + E_{\text{potLigand}} \\ + E_{\text{solvLigand}} - E_{\text{potComplex}} - E_{\text{solvComplex}}$$

Here, YASARA built-in macros was used to calculate MM-PBSA binding energy, using AMBER 14 as a force field, where more positive energies indicate better binding [53].

Results and discussion

Virtual screening

Overexpression of VEGF and its receptor VEGFR-2 is the most common phenomenon in angiogenesis and plays a significant role in cell survival and promoting tumorigenesis

[54–56]. In current drug discovery processes, virtual screening is the most widely used approach to find novel hits for a target by reducing time, cost and the massive compound library. Apparently, XP docking assists in filtering out false positives from the compound database by using a strict scoring function; hence, it was considered in this study [57]. However, prior to docking simulations, we first validated docking accuracy through redocking of a known reference ligand using XP docking methodology. Here, the reference co-crystal ligand was first separated and re-docked using the Glide XP algorithm. Conformation of the complex with the highest negative docking score was selected from each run. The RMSD of the docked conformation was then calculated, where a lower RMSD value denotes a high level of the accuracy of docking protocol. Interestingly, Glide docking with XP setting produced the docked complex with lowest RMSD of 0.61 Å, which denoted that the position of docked ligand was almost similar to that of the crystal, as shown in Fig. S2 (see supplementary file 1). Therefore, the candidate ligands including reference inhibitors, sunitinib and sorafenib were docked into VEGFR-2, following the same docking protocol.

Initially, the top 5% compounds were selected from Glide XP docking based on high docking score. As a result, 35 compounds were considered, with docking score range from -12.00 to -10.00 kcal mol⁻¹, in which the highest docking score was found to be -11.80 kcal mol⁻¹ for **ZINC95099443** and the lowest docking score was -10.04 kcal mol⁻¹ for **ZINC95099251**. On the contrary, the reference inhibitors, sunitinib and sorafenib resulted in docking scores of -6.60 kcal mol⁻¹, and -7.65 kcal mol⁻¹, respectively (Table 1). However, bioavailability and toxicity are the primary concerns for drug development; therefore, we subjected these compounds for ADME/T profiling, as discussed below.

Bioavailability of ligands

Pharmaceutically relevant attributes and physiochemical descriptors of the identified hypothetical hits were calculated by QikProp software. Each descriptor's range satisfies 95% of

known drugs [58–60]. The pharmacokinetic properties of 35 ligands were assessed (see supplementary file 2), where cell permeability, the number of rotatable bonds, number of metabolites, solubility, logP, and oral absorption rate were predicted, from which the top six candidates were selected (Fig. S3, see supplementary file 1).

As described in Table 2, all calculated attributes were in the satisfactory range, with properties including, QPlogPo/w (octanol/water partition coefficient), QPlogHERG (log IC₅₀ value for blockage of K⁺ channels) [61, 62], SASA [59], QPlogS (aqueous solubility) [59], molecular weight, and H bond acceptor/donor [61]. Although the standard inhibitors obtained highest oral absorption, they were also predicted to fall outside the recommended range for QPlogHERG value. The HERG K⁺ channel, which is encoded by the human ether-a-go-go related gene (HERG), is one of the main reasons for the cardiac toxicity produced by a wide range of therapeutic drugs [63]. This channel promotes electrical activity of the heart and also modulates various functions of the nervous system [64]; thus, blockers of this channel cause potential toxicity, which is a major consideration in drug discovery processes [65]. All these findings indicating that the ligands identified showing ideal behavior of drug molecules, and that they are well tolerated and less toxic than standard inhibitors.

MM-GBSA binding affinity estimation

The top six identified ligands were re-ranked by their binding affinity calculated through MM-GBSA analysis: **ZINC14762520** obtained highest binding affinity ($\Delta G_{\text{Bind}} = -78.09$ kcal mol⁻¹) with highest contribution from covalent and lipophilic binding energies. In contrast, **ZINC95099475** showed the lowest binding affinity of -58.29 kcal mol⁻¹ (Table S1, see supplementary file 1). In comparison to the identified ligands, the reference inhibitors sunitinib and sorafenib showed binding affinities of -45.26 kcal mol⁻¹ and -57.44 kcal mol⁻¹ respectively. On the basis of MM-GBSA result, we thus selected the top four compounds and subjected them to detailed binding analysis.

Table 1 Top six candidates generated from structure based virtual screening on the basis of extra precision (XP) Glide docking against VEGFR-2

Compound name	Docking score (kcal mol ⁻¹)	Glide energy (kcal mol ⁻¹)	Glide ligand efficiency	Strain penalty	Glide Emodel (kcal mol ⁻¹)
Sunitinib	-6.60	-51.69	-0.22	0	-72.91
Sorafenib	-7.65	-53.60	-0.23	0	-88.69
ZINC13370550	-10.68	-55.73	-0.35	0	-88.02
ZINC02585769	-10.64	-44.22	-0.50	0	-70.24
ZINC95099475	-10.19	-42.89	-0.48	0	-65.61
ZINC36470466	-11.06	-48.05	-0.48	0	-66.98
ZINC38957372	-11.43	-43.63	-0.54	0	-69.10
ZINC14762520	-10.64	-34.85	-0.39	0	-70.95

Table 2 Pharmacokinetic and toxicological properties of the top six candidates and standard inhibitors, calculated from QikProp

Name	MW ^a	HB donor ^b	HB acceptor ^c	SASA ^d	log HERG ^e	Qlog S ^f	log Po/w ^g	% Human oral absorption ^h
Sunitinib	398.47	2.00	6.00	751.53	-6.68	-5.32	3.84	89.98
Sorafenib	464.83	3.00	6.00	748.03	-5.64	-6.97	3.94	96.88
ZINC13370550	416.38	4	10.55	660.94	-5.006	-3.66	0.59	59.78
ZINC02585769	286.24	4	5.5	496.06	-4.097	-2.53	0.44	60.22
ZINC95099475	288.25	3	4.75	494.56	-4.676	-2.90	0.95	65.55
ZINC36470466	318.36	5	5.65	578.41	-5.003	-2.44	1.37	65.62
ZINC38957372	290.27	4	5.5	523.10	-5.047	-2.59	0.90	66.99
ZINC14762520	372.41	3	4.75	661.36	-5.000	-4.34	3.2	84.28

^a Molecular weight (acceptable range: <500)

^b Hydrogen bond donor (acceptable range: ≤5)

^c Hydrogen bond acceptor (acceptable range: ≤10)

^d Total solvent accessible surface area in using a probe with a 1.4 radius (acceptable range: 300–1000)

^e Predicted IC50 value for blockage of HERG K⁺ channels (concern: below -5)

^f Predicted aqueous solubility, S in mol dm⁻³ (acceptable range: -6.5 to 0.5)

^g Predicted octanol/water partition coefficient (acceptable range: -2 to 6.5)

^h Predicted human oral absorption on 0 to 100% scale (<25% is poor and >80% is high)

Ligand binding analysis

The docked complexes of the top four virtual hits from Glide XP docking were further considered for protein–ligand interaction profiling. As shown in Table 3, and Fig. 1a, **ZINC02585769** showed four hydrogen bonds with C⁹¹⁹, D¹⁰⁴⁶, E⁸⁸⁵ and G⁹²² residues, while C⁹¹⁹ formed double hydrogen bonds with the ligand, maintaining corresponding bonding distances of 2.23 Å and 2.41 Å, respectively. Although the ligand formed major hydrophobic interactions with K⁸⁶⁸, V⁸⁹⁹, V⁸⁴⁸, L⁸⁴⁰, A⁸⁶⁶ and L¹⁰³⁵ through pi-alkyl bonding, C⁹¹⁹ and K⁹²⁰ showed additional amide-pi stacking interactions with the ligand.

On the other hand, **ZINC13370550** (Fig. 1b) formed several hydrogen bonds with the active site residues, where most of the interactions were mediated by E⁸⁶⁸, C⁹¹⁹ and N⁹²³ residue. C⁹¹⁹ was also involved in π-donor hydrogen bonding with the ligand, while L⁸⁴⁰, L¹⁰³⁵, V⁸⁴⁸, A⁸⁶⁶ and C¹⁰⁴⁵ were responsible for hydrophobic interactions via π-alkyl bonding.

In the case of the **ZINC14762520**-VEGFR-2 complex, **ZINC14762520** showed hydrogen bonding to the active site, where the interactions were maintained by C⁹¹⁹, D¹⁰⁴⁶ and F¹⁰⁴⁷ residues. Furthermore, **ZINC14762520** also formed pi-alkyl bonds with K⁸⁶⁸, V⁸⁹⁹, A⁸⁶⁶, C⁹¹⁹ and L¹⁰³⁵ residues and were thus involved in hydrophobic interactions (Fig. 1c).

ZINC36470466 (Fig. 1d) formed a stable complex with VEGFR-2 by forming hydrogen bonds with T⁹¹⁶, D¹⁰⁴⁶ and C⁹¹⁹ side chains, where both D¹⁰⁴⁶ and C⁹¹⁹ showed two hydrogen bonds individually. Here, V⁸⁹⁹, L⁸⁴⁰, V⁸⁴⁸, A⁸⁶⁶ and L¹⁰³⁵ were involved in hydrophobic interactions by π-alkyl interactions.

According to the detailed analysis of molecular interactions, except **ZINC14762520**, all compounds formed hydrophobic interactions with L⁸⁴⁰ and L⁸⁴⁸ residues of the glycine rich loop (G-loop) that makes a hydrophobic interaction with ATP [66, 67], while **ZINC14762520** showed interactions with several residues from the hinge region and DFG motif, including C⁹¹⁹, D¹⁰⁴⁶ and F¹⁰⁴⁷. All ligands also made contacts with the residues of the linker region, including C¹⁰⁴⁵ and D¹⁰⁴⁶, which confirms their VEGFR-2 inhibition, as these residues are directly involved in polar interactions with ATP, assist the shifting of γ-phosphate through coordinating Mg²⁺ ions [68]. Furthermore, non-covalent interactions of the residues of the hinge region (T⁹¹⁷ to N⁹²³) with all four ligands revealed that these compounds may act as ATP competitive inhibitors [69, 70].

MD simulations

To describe the binding mechanisms, flexibilities and structural behaviors of the top virtual hits, we conducted MD simulations for 100 ns for each complex, including the reference inhibitor, sunitinib and also the ligand free protein. Different energies such as coulomb, van der Waals and total energies were calculated for each system (summarized in Table S2). The atomic RMSDs of the Cα, C, and N atoms of protein in all complexes were calculated from the simulation trajectories and are plotted in Fig. 2. As shown in Fig. 2, the highest RMSD values were observed for **ZINC36470466**, while **ZINC02585769** obtained the lowest RMSDs in the 100 ns simulation. As can be seen from the plot, **ZINC02585769** showed a more rigid conformation than the other proteins, and also achieved equilibrium at 10 ns and remained stable afterward.

Table 3 Detailed molecular interactions analysis for best hits obtained from Glide XP docking

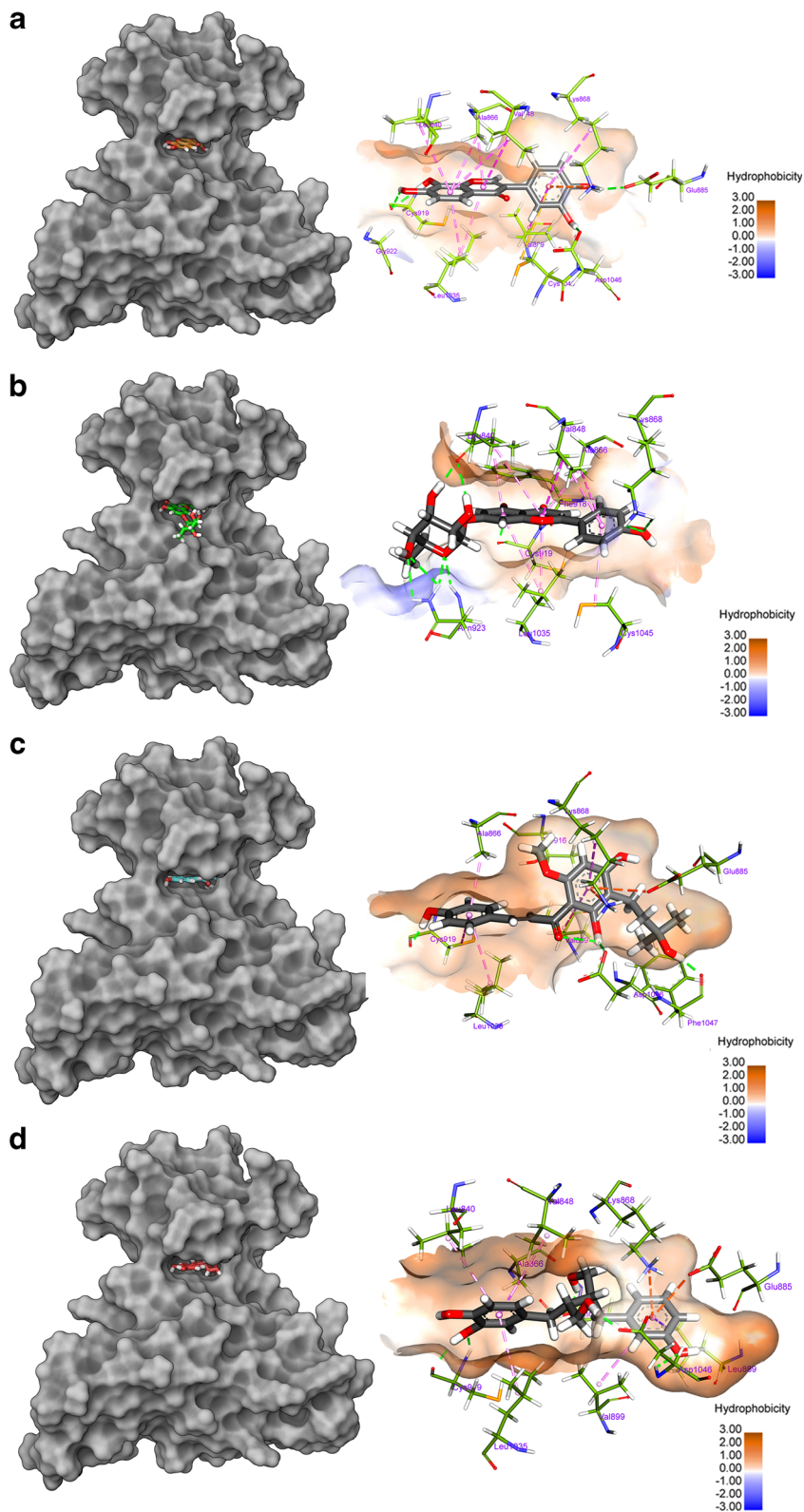
Compound	Conventional hydrogen bonds	π -Donor hydrogen bond	Hydrophobic	
			π -Alkyl	Amide- π -stacked
ZINC02585769	C ⁹¹⁹ (2.23 Å),		K ⁸⁶⁸ (5.15 Å),	C ⁹¹⁹
	C ⁹¹⁹		V ⁸⁹⁹	(4.18 Å),
	D ¹⁰⁴⁶ (2.41 Å),		V ⁸⁴⁸ (4.88 Å),	K ⁹²⁰
	(1.88 Å),		(4.73 Å),	(4.18 Å)
	E ⁸⁸⁵ (2.15 Å)		A ⁸⁶⁶ (3.76 Å),	
			L ¹⁰³⁵ (4.46 Å),	
			L ⁸⁴⁰ (5.02 Å),	
			V ⁸⁴⁸ (5.31 Å),	
			A ⁸⁶⁶ (4.94 Å),	
			L ¹⁰³⁵ (4.41 Å)	
ZINC13370550	E ⁸⁶⁸ (2.83 Å),	C ⁹¹⁹	L ⁸⁴⁰ (4.36 Å),	
	E ⁸⁶⁸	(3.13 Å)	L ¹⁰³⁵	
	(2.90 Å),		(5.12 Å),	
	C ⁹¹⁹		L ⁸⁴⁰	
	(2.05 Å),		(5.33 Å),	
	N ⁹²³		V ⁸⁴⁸	
	(2.26 Å),		(4.92 Å),	
	N ⁹²³		A ⁸⁶⁶	
	(2.52 Å),		(4.16 Å),	
	N ⁹²³		L ¹⁰³⁵	
(2.23 Å),		(4.52 Å),		
N ⁹²³		V ⁸⁴⁸		
(2.62 Å),		(4.65 Å),		
C ⁹¹⁹		A ⁸⁶⁶		
(1.83 Å),		(5.29 Å),		
L ⁸⁴⁰		C ¹⁰⁴⁵		
(2.15 Å),		(4.60 Å)		
L ⁸⁴⁰				
(1.87 Å)				
ZINC14762520	C ⁹¹⁹ (1.98 Å),		K ⁸⁶⁸ (4.60 Å),	
	D ¹⁰⁴⁶		V ⁸⁹⁹	
	(2.10 Å),		(5.35 Å),	
	C ⁹¹⁹		A ⁸⁶⁶	
	(1.82 Å),		(3.86 Å),	
	F ¹⁰⁴⁷		C ⁹¹⁹	
	(1.64 Å)		(4.94 Å),	
		L ¹⁰³⁵		
		(4.51 Å)		
ZINC36470466	C ⁹¹⁹ (1.91 Å),		V ⁸⁹⁹ (5.19 Å),	
	D ¹⁰⁴⁶		L ⁸⁴⁰	
	(2.09 Å),		(5.07 Å),	
	T ⁹¹⁶		V ⁸⁴⁸	
	(2.12 Å),		(5.15 Å),	
	C ⁹¹⁹		A ⁸⁶⁶	
	(1.98 Å),		(4.43 Å),	
D ¹⁰⁴⁶		L ¹⁰³⁵		
(1.96 Å)		(4.52 Å),		

In contrast, **ZINC36470466** showed a dramatic increase in flexibility, with RMSD values rising gradually from 1.5 Å to 2.75 Å over time. **ZINC14762520** was in equilibrium up to 70 ns, but showed fluctuations thereafter. On the other hand, the apo form also reached at equilibrium after 10 ns and maintained

RMSD up to 1.9 Å for 50 ns, after which the RMSD was seen to increase gradually. Similarly, sunitinib displayed stable RMSD up to 50 ns; however, after that it decreased to 1.5 Å and remained steady thereafter. Overall, the results of RMSD analysis clearly depicted that the conformation of the protein was changed upon ligand binding, as the apo structure represented the lowest RMSD fluctuations over the course of the simulation. In order to investigate local fluctuations in protein structure induced by the ligands, the root mean square fluctuation (RMSF) of each protein backbone was calculated. As shown in Fig. 3a, five flexible regions were involved in the ATP binding site, including G-loop L⁸³⁶ to I⁸⁴⁹, hyd-1 A⁸⁶⁶ to K⁸⁶⁸, hinge T⁹¹⁶ to N⁹²³, catalytic subunit H¹⁰²⁶ to L¹⁰³⁵ and DFG motif C¹⁰⁴⁵ to G¹⁰⁴⁸. Among these compounds, **ZINC36470466** produced the highest fluctuations in G-loop regions, while **ZINC14762520** showed low RMSF compared to the apo form. Again in all cases, amino acids ranging from 114 to 128 fluctuated more in apo form; however, fluctuations were seen to reduce after ligand binding. In the case of the standard inhibitor, sunitinib increased flexibility in the hinge region, up to 1.9 Å, while no significant changes in RMSF were observed for **ZINC14762520**. It is also noteworthy that binding of all ligands except **ZINC14762520** increased local fluctuations of the catalytic subunit region in comparison to the apo protein. This was due to their strong interactions with residues and rotation of the particular pharmacophore involved in intermolecular interactions. In the DFG motif, **ZINC13370550** produced the highest RMSF, which denotes increased flexibility in this region. Overall, RMSF analysis suggested that all compounds formed favorable interactions with ligand binding regions. Although dynamic changes occurred upon binding to these ligands, protein stability was increased, which is similar to the reference ligand.

To further clarify the structural deviation derived by the ligands, flexibilities of the protein in terms of SASA, radius of gyration and number of hydrogen bond were calculated. Figure 4 depicts the total SASA of each protein, i.e., the biomolecular surface area that is assessable to solvent molecules. Here, decreased values of SASA denotes the shrunken nature [71]. The results of SASA analysis suggest that **ZINC02585769** increased the SASA of protein with several large fluctuations in 100 ns simulation. Conversely, **ZINC13370550** showed a pattern similar to that of the standard inhibitor sunitinib, indicates that **ZINC13370550** was dynamic over the simulation. Comparatively, **ZINC36470466** showed lower SASA values over time, allowing us to conclude that the ligand caused tight packing of the protein. Interestingly, **ZINC14762520** maintained a steady SASA profile over time; however, some large fluctuations were seen in 100 ns of simulation. On the other hand, the radius of gyration of the proteins, shown in Fig. 5a, revealed that **ZINC14762520** produced a higher radius of gyration at the beginning, which was then maintained over the entire

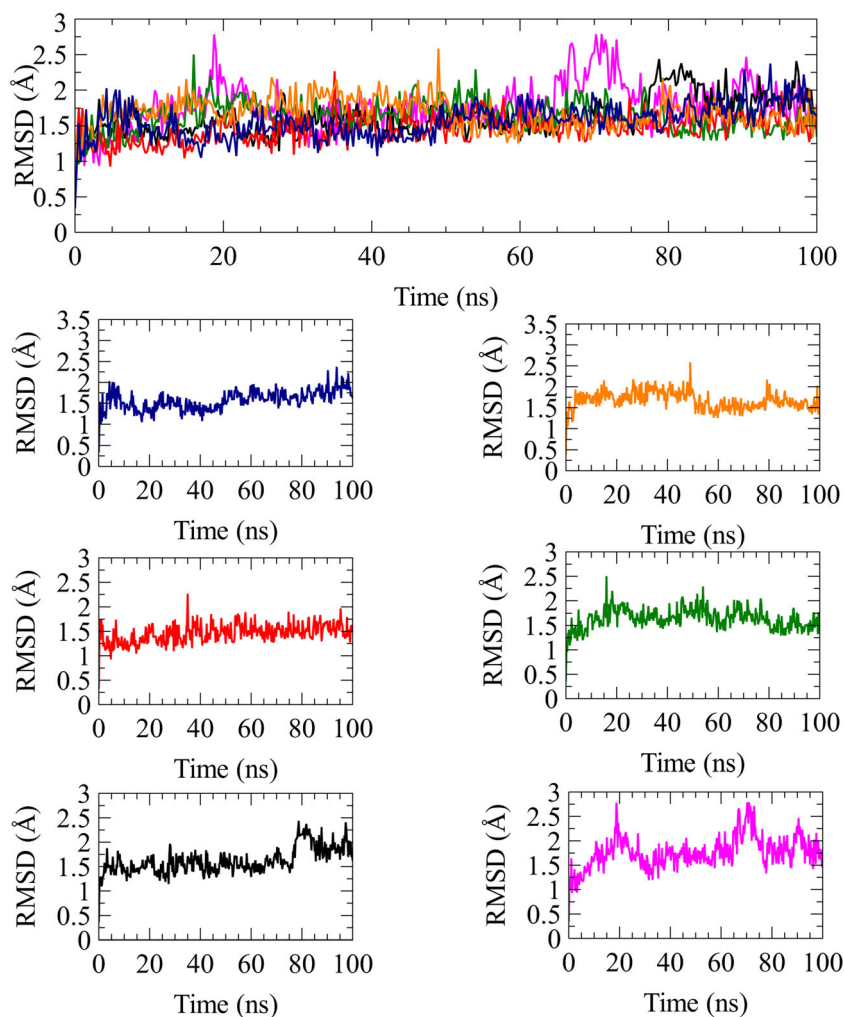
Fig. 1a–d Binding modes of compounds with VEGFR-2. Molecular interactions are displayed in hydrophobic surface view. Green dotted line Hydrogen bonds, pink dotted lines π -alkyl interactions. The hydrophobic intensities of the binding site ranged from -3.00 (least hydrophobic area—shaded blue) to 3.00 (highly hydrophobic area—shaded brown). **a** ZINC02585769, **b** ZINC13370550, **c** ZINC14762520, **d** ZINC36470466



simulation time. In comparison to the other ligands, **ZINC36470466** showed lower values; these results therefore suggest flexibility of **ZINC14762520** as well as tight packing of **ZINC36470466**, as higher radius of gyration value denotes

loose packing of the protein structure, which clearly supports the results calculated from SASA analysis. In addition, sunitinib maintained a radius of gyration profile similar to that of the apo state after 17 ns; no significant changes were seen

Fig. 2 Time evolution of root-mean-square deviations (RMSDs) of backbone atoms (C, C α , and N) for protein of each docked complex. Complexes: *Blue* apo, *orange* sunitinib, *red* ZINC02585769, *olive green* ZINC13370550, *black* ZINC14762520, *pink* ZINC36470466



thereafter. Figure 5b represents the total intra-residue hydrogen bonds formed during the simulations, in which maximum highest picks were observed for apo form and ZINC14762520. On average, there was insignificant variation of hydrogen bonding among the proteins, ranging from 50 to 100 (Table S2, see supplementary file 1). Nevertheless, it is concluded that binding of ligands, including standard inhibitors, reduced intra-residue hydrogen bonds in the protein, therefore increasing flexibility. The degree of flexibility increased by binding of ZINC13370550 and thus the overall dimension of the structure was enhanced, while it was reduced by the binding of ZINC36470466. The total number of H-bonds between the ligand and residues of the ATP binding site of protein for each complex are represented in Fig. 6, where maximum hydrogen bonding was observed for ZINC36470466 (Fig. 6e) during the simulation, while ZINC13370550 (Fig. 6c) showed minimum interaction (Table 2). For a detailed understanding, H-bond occupancy was calculated and represented in Fig. 6f. Here Fig. 6f shows the percentage of H-bond occupancy, where each residue either acted as a donor or as an acceptor.

As shown in Fig. 6f, ZINC14762520 formed several H-bonds with the residues of DFG motif and hinge region, including C⁹¹⁹, E⁸⁸⁵, F¹⁰⁴⁷ and D¹⁰⁴⁶ residues during the simulation, with total occupancy of more than 15%. The major interaction with C⁹¹⁹ was mediated by the hydroxyl group present in the 4-hydroxyphenyl part of ZINC14762520, where the oxygen atom acted as acceptor. ZINC36470466 formed H-bonds with D¹⁰⁴⁶ and E⁸⁸⁵ residues as H-bond donor, occupying more than 50% of the simulation, while less than 20% of H-bonds were occupied as acceptor with C⁹¹⁹ residue. Here, hydroxyl groups present at the 3-hydroxybenzyl part of the compound act as donors in the interactions with D¹⁰⁴⁶ residues of DFG motif. The main contribution of ZINC02585769 in the hydrogen bonding interaction was with residue E⁸⁸⁵, with 121.04% H-bond occupancy. The hydroxyl groups present at the 3,4-dihydroxyphenyl part are major contributors in H-bond formation, acting as donors. In contrast, ZINC13370550 showed maximum H-bond occupancy with T⁹²⁶ and C⁹¹⁹ residues as both H-bond donor and acceptor, with interaction maintained by

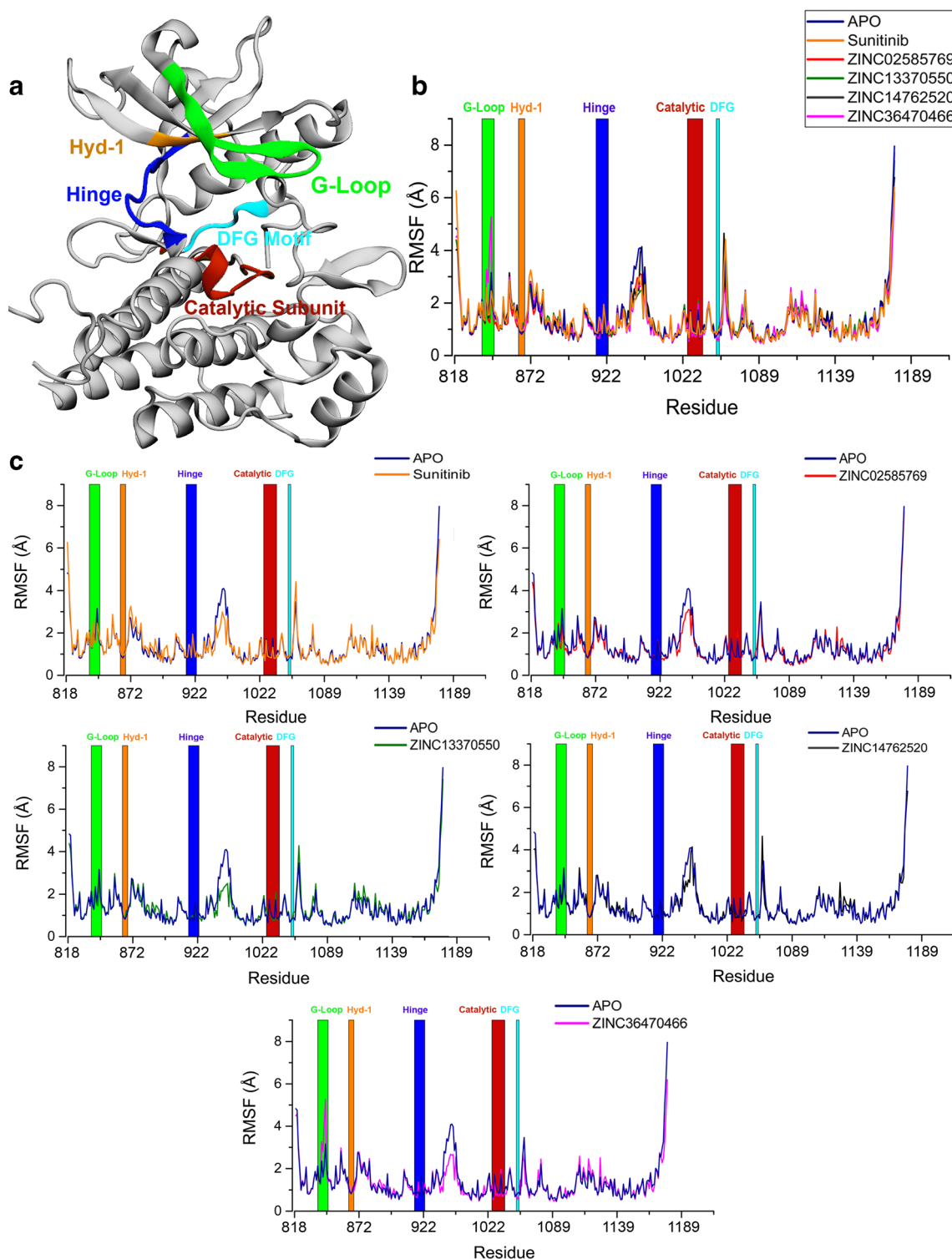


Fig. 3 **a** Structural representation of VEGFR-2 kinase highlighting the different motifs involved in ATP binding. **b** Root mean square fluctuation (RMSF) plots of protein–ligand complexes: *Blue* apo, *orange* sunitinib, *red* ZINC02585769, *olive green* ZINC13370550, *black*

ZINC14762520, *pink* ZINC36470466. **c** Comparative RMSF plot between protein–ligand complexes and apo structure. Residues involved: *light green* G-loop, *orange* hyd-1, *blue* hinge, *brick red* catalytic subunit, *cyan* DFG motif

the d-glucopyranose ring and ketone group present in the flavones part, respectively. Sunitinib interacted with residue E⁹¹⁷ more than 35% as a donor with an additional H-

bond with L⁸⁴⁰ having a percentage occupancy of around 10%. As an acceptor, sunitinib maintained H-bonds with C⁹¹⁹ residues about 34% of total simulation time.

Fig. 4 Ligand-induced thermodynamic behavior of protein during simulations. The plots describe structural changes of protein by means of solvent accessible surface area (SASA). Complexes: *Blue* apo, *orange* sunitinib, *red* ZINC02585769, *olive green* ZINC13370550, *black* ZINC14762520, *pink* ZINC36470466

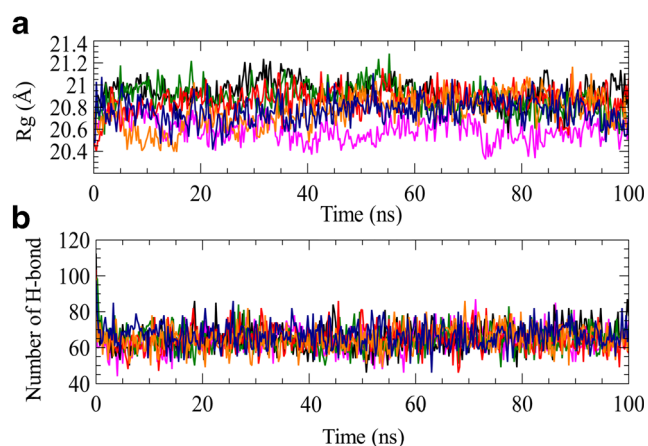
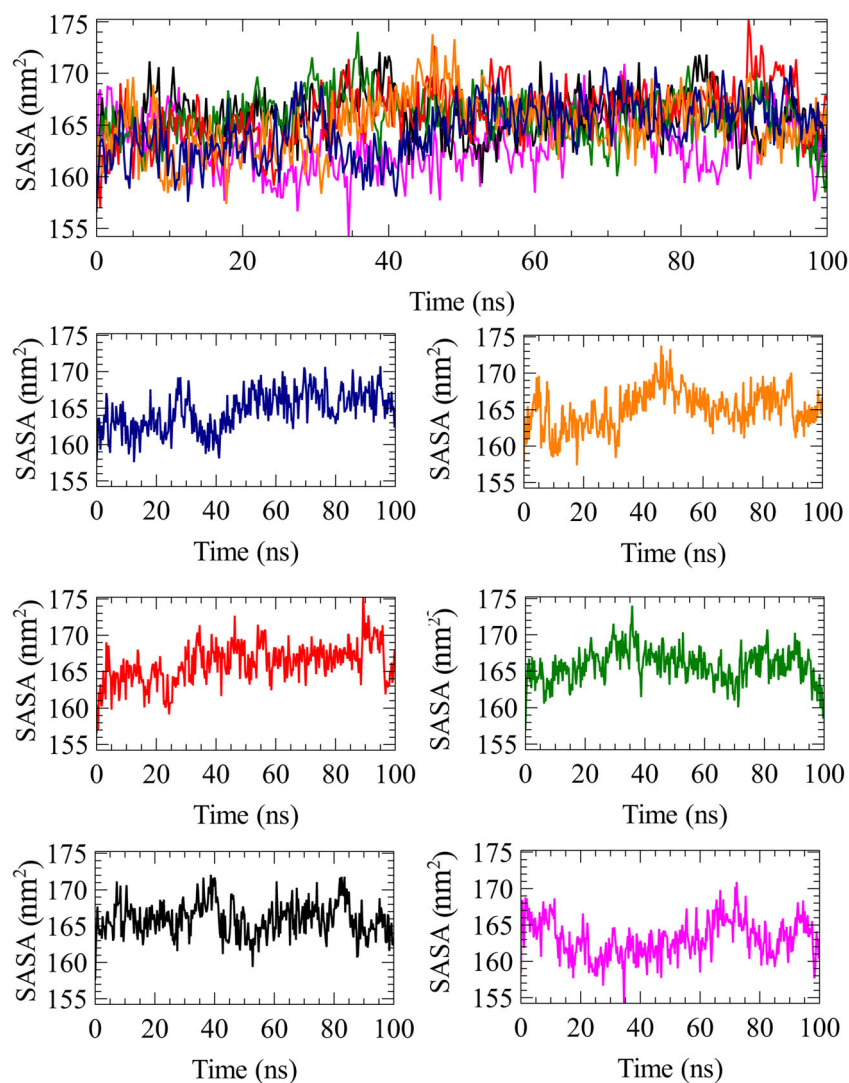
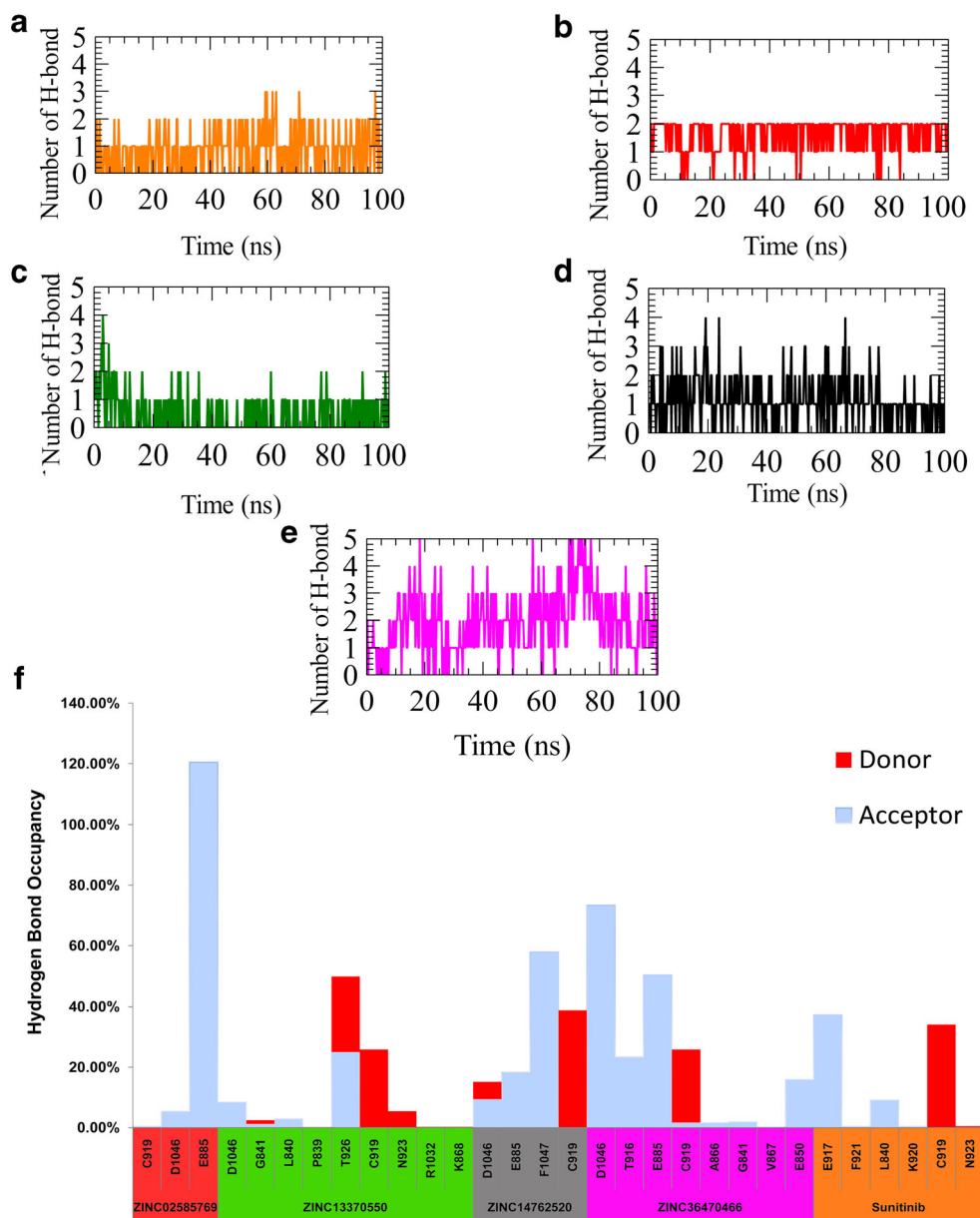


Fig. 5 Time evolution of **a** radius of gyration, and **b** total number of hydrogen bonds formed within the protein during 100 ns of MD simulations. Complexes: *Blue* apo, *orange* sunitinib, *red* ZINC02585769, *olive green* ZINC13370550, *black* ZINC14762520, *pink* ZINC36470466

In computer-aided drug design approaches, Poisson-Boltzmann surface area (PBSA) is one of most attractive solvation systems that is applied widely to calculate binding energy of protein–ligand complexes [51, 72]. Hence, we subjected each protein–ligand complex to a MM-PBSA binding energy calculation to see how structural changes influence ligand binding. With this aim, we calculated the binding energy of every snapshot produced from MD simulations. The results are plotted in Fig. 7a, where more positive energies indicated better binding, according to the theory of nuclear physics [73]. According to the laws of physics, the energy required to disassemble a whole into separate parts is usually positive [74]. On average, ZINC14762520 obtained maximum energy of binding of $166.12 \pm 6.5 \text{ kJ mol}^{-1}$, while ZINC02585769 showed the least energy of $19.45 \pm 1.4 \text{ kJ mol}^{-1}$. The reference inhibitor exhibited a binding energy of $115.43 \pm 1.2 \text{ kJ mol}^{-1}$. By contrast, the ZINC13370550 and

Fig. 6a–f Total number of hydrogen bonds formed between protein and ligand in complex state during the simulation. **a** Sunitinib, **b** ZINC02585769, **c** ZINC13370550, **d** ZINC14762520, **e** ZINC36470466. **f** Percentage occupancy of hydrogen bond formed between the ligands and active site residues, showing the time evolution of the occupancy of the listed hydrogen bonds, where each residue either acted as donor or acceptor in hydrogen bonding with ligand

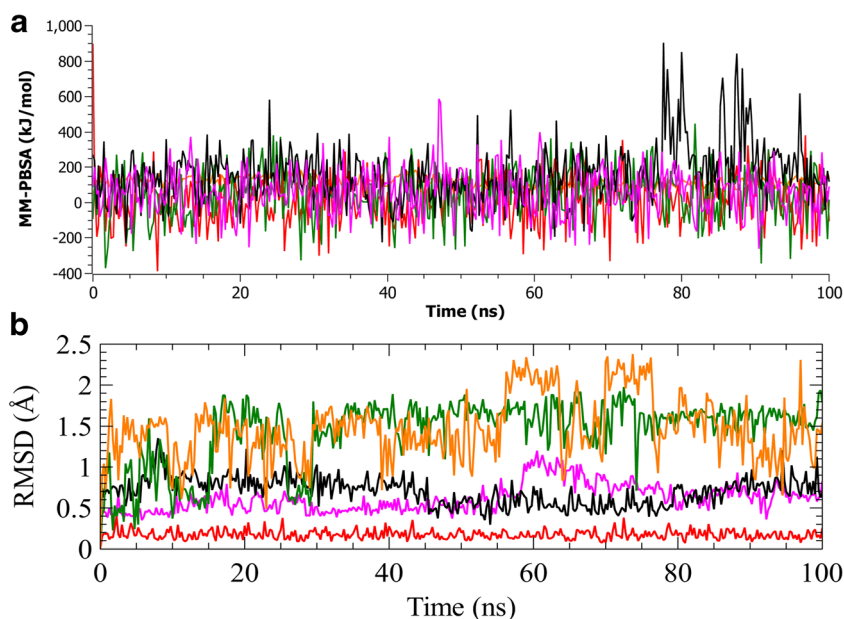


ZINC36470466 complexes showed positive binding energy values of $49.52 \pm 5.2 \text{ kJ mol}^{-1}$ and $60.92 \pm 4.7 \text{ kJ mol}^{-1}$, respectively.

Although ZINC02585769 produced higher binding energy at initial stages of simulation, the binding energy was seen to decrease afterward. ZINC36470466 and ZINC14762520 showed similar patterns of binding energy profiles; however, ZINC36470466 obtained lower binding energy after 50 ns of simulation. As ligand flexibility is involved in the formation and breakdown of new bonds in the active site, we analyzed ligand RMSD to gain more detailed understanding. As shown Fig. 7b, the conformation of the sunitinib fluctuated up to 2.4 Å, and several large decreases in fluctuation were observed one by one over time. Despite several fluctuations, sunitinib maintained binding energy above 40 kJ mol^{-1} in total time of

MD simulation. Likewise, over the course of simulation, ZINC14762520 supported stable conformations with RMSD up to 0.7 Å, although several oscillations were observed, which therefore caused variations in binding energy. With regard to ZINC13370550, the ligand showed conformational shifting at 19 ns, which thus produced higher binding energy at that time; however, several large shifting occurred afterward which indicates greater fluctuation in binding energy profile. As a result, these conformational shifts caused weaker binding of the ligand with the active site residues of the protein, therefore resulting in low MM-PBSA binding free energy, as can be observed in Fig. 7a. On the other hand, ZINC02585769 showed a rigid conformation over time, thus showing that flexibility of the ligand plays an important role in the formation of a stable protein–ligand complex.

Fig. 7 **a** Binding free energy (in kJ mol^{-1}) of each snapshot was calculated by molecular mechanics Poisson-Boltzmann surface area (MM-PBSA) analysis, representing the change in binding stability of each complex during simulations; positive values indicate better binding. **b** Time evolution of root-mean-square deviations (RMSDs) of ligand for each docked complex. Complexes: *Blue* apo, *orange* sunitinib, *red* ZINC02585769, *olive green* ZINC13370550, *black* ZINC14762520, *pink* ZINC36470466



Overall, MD trajectory analysis infers that **ZINC14762520** and **ZINC36470466** are the most potent candidates among the herbal secondary in vivo metabolites to inhibit VEGFR-2 kinase. Both these compounds achieved highest average binding free energies in MM-PBSA analysis among the top virtual hits, and the binding energy of **ZINC14762520** was greater than the reference inhibitor sunitinib. They also maintained maximum non-covalent interactions in 100 ns with residues of the three most important ligand binding regions in VEGFR-2 kinase, including G-loop, DFG motif and hinge regions [75]. In all kinase domains, G-loop and hinge regions serve as important components for ligand binding, where the G-loop interacted with the purine ring of adenine, and the hinge region acts as the ribose binding pocket [76]. Interestingly, both compounds **ZINC14762520** and **ZINC36470466** interacted with the residues involved in the hinge region and the DGF motif. Comparatively, **ZINC36470466** sustained maximum interactions with hinge regions by its benzyl rings, although **ZINC14762520** contains a hydroxyl pharmacophore in the 4-hydroxyphenyl portion that stabilized hinge binding by hydrogen bonding more than 35% in total simulation (Fig. 3f). Furthermore, docking analysis showed that **ZINC36470466** formed hydrophobic interactions through its aromatic ring with L⁸⁴⁰ and V⁸⁴⁸ residues of the G-loop region. Hence, we calculated the atomic distances between the interacting ring of the ligands and the beta carbon of L⁸⁴⁰ and V⁸⁴⁸ residues, respectively. As shown in Fig. S4 (see supplementary file 1), **ZINC36470466** maintained distances less than 5.5 Å in 100 ns simulation with these hydrophobic residues, despite exhibiting some fluctuation. Furthermore, L⁸⁴⁰ maintained maximum intermolecular distance with the ligand from 4 to 5.5 Å in the total simulation, which indicates that L⁸⁴⁰ of the G-loop contributed stronger

hydrophobic interaction than V⁸⁴⁸. Taken together, the above analysis suggests strong stability and VEGFR-2 kinase inhibition with both **ZINC14762520** and **ZINC36470466**.

Conclusion

In this in silico experiment, we tried to identify potent inhibitors of VEGFR-2 from a database of in vivo metabolites of herbal ingredients, using Glide XP docking and ADME/T analysis to identify the six best candidates. Among them, the top four virtual hits were specified by MM-GBSA calculations. And finally, **ZINC14762520** and **ZINC36470466** have been selected as the best virtual hits by MM-PBSA and MD simulations. Molecular docking analysis revealed the detailed binding mode of the selected virtual hits with VEGFR-2. According to MD simulation analysis, these compounds energetically formed stable complexes with VEGFR-2 kinase owing to different conformational changes. In addition, all identified compounds were predicted to be orally active and satisfied a drug likeness profile. Compared to standard inhibitors, they are also predicted to be less susceptible to cardiac toxicity. The results of this study therefore offer a suitable starting point for further development as well as detailed in vitro and in vivo analyses.

Acknowledgments We thank Dr. Elmar Krieger, YASARA Biosciences GmbH, for providing an academic version of YASARA dynamics software. The authors acknowledge Prof. Gert Vriend (WHAT IF Foundation / CMBI, Netherlands) for his critical suggestions in Protein Dynamics Simulations. The authors are grateful to the Bangladesh Council of Scientific and Industrial Research for funding under the R&D project (SL. No. 42, 2016-17) to build a computational platform in Bangladesh.

Author contributions R. D., S.M., S.M.Z.H. and M. A. planned experiments, analyzed data and prepared manuscript. R.D. S.M. and M. J performed experiments, and prepared the figures. All authors reviewed the manuscript.

Compliance with ethical standards

Competing financial interests The authors declare no competing financial interests.

References

- Luo H, Jiang B-H, King SM, Chen YC (2008) Inhibition of cell growth and VEGF expression in ovarian cancer cells by flavonoids. *Nutr Cancer* 60(6):800–809
- Tsuzuki Y, Carreira CM, Bockhorn M, Xu L, Jain RK, Fukumura D (2001) Pancreas microenvironment promotes VEGF expression and tumor growth: novel window models for pancreatic tumor angiogenesis and microcirculation. *Lab Invest* 81(10):1439–1451
- Aziz MA, Serya RAT, Lasheen DS, Abdel-Aziz AK, Esmat A, Mansour AM, Singab ANB, Abouzid KAM (2016) Discovery of potent VEGFR-2 inhibitors based on furopyrimidine and thienopyrimidine scaffolds as Cancer targeting agents. *Sci Rep* 6: 24460. <https://doi.org/10.1038/srep24460>
- Plate KH, Breier G, Weich HA, Risau W (1992) Vascular endothelial growth factor is a potential tumour angiogenesis factor in human gliomas in vivo. *Nature* 359(6398):845
- Raju D, Junaid NI, Forhad Chowdhury A, Imran K, Arifuzzaman MK, Hosen SMZ (2017) Molecular insight and binding pattern analysis of Shikonin as a potential VEGFR-2 inhibitor. *Curr Enzym Inhib* 13:1–10. <https://doi.org/10.2174/1573408013666161227162452>
- Takahashi H, Shibuya M (2005) The vascular endothelial growth factor (VEGF)/VEGF receptor system and its role under physiological and pathological conditions. *Clin Sci* 109(3):227–241
- Gerhardt H, Golding M, Fruttiger M, Ruhrberg C, Lundkvist A, Abramsson A, Jeltsch M, Mitchell C, Alitalo K, Shima D (2003) VEGF guides angiogenic sprouting utilizing endothelial tip cell filopodia. *J Cell Biol* 161(6):1163–1177
- Hosen SZ, Dash R, Khatun M, Akter R, Bhuiyan MHR, Rezaul M, Karim NJM, Ahamed F, Islam KS, Afrin S (2017) In silico ADME/T and 3D QSAR analysis of KDR inhibitors. *J Appl Pharmaceut Sci* 7:120–128
- Yoshihara T, Takahashi-Yanaga F, Shiraishi F, Morimoto S, Watanabe Y, Hirata M, Hoka S, Sasaguri T (2010) Anti-angiogenic effects of differentiation-inducing factor-1 involving VEGFR-2 expression inhibition independent of the Wnt/ β -catenin signaling pathway. *Mol Cancer* 9:245–245. <https://doi.org/10.1186/1476-4598-9-245>
- Mamluk R, Carvajal IM, Morse BA, Wong H, Abramowitz J, Aslanian S, Lim A-C, Gokemeijer J, Storek MJ, Lee J, Gosselin M, Wright MC, Camphausen RT, Wang J, Chen Y, Miller K, Sanders K, Short S, Sperinde J, Prasad G, Williams S, Kerbel R, Ebos J, Mutsaers A, Mendlein JD, Harris AS, Furfine ES (2010) Anti-tumor effect of CT-322 as an adnectin inhibitor of vascular endothelial growth factor receptor-2. *mAbs* 2(2):199–208
- Faivre S, Demetri G, Sargent W, Raymond E (2007) Molecular basis for sunitinib efficacy and future clinical development. *Nat Rev Drug Discov* 6(9):734–745. <https://doi.org/10.1038/nrd2380>
- Kamba T, McDonald D (2007) Mechanisms of adverse effects of anti-VEGF therapy for cancer. *Br J Cancer* 96(12):1788–1795
- Noble ME, Endicott JA, Johnson LN (2004) Protein kinase inhibitors: insights into drug design from structure. *Science* 303(5665): 1800–1805. <https://doi.org/10.1126/science.1095920>
- Gotink KJ, Verheul HMW (2010) Anti-angiogenic tyrosine kinase inhibitors: what is their mechanism of action? *Angiogenesis* 13(1): 1–14. <https://doi.org/10.1007/s10456-009-9160-6>
- Amin AR, Kucuk O, Khuri FR, Shin DM (2009) Perspectives for cancer prevention with natural compounds. *J Clin Oncol* 27(16): 2712–2725
- Schieber A, Stintzing F, Carle R (2001) By-products of plant food processing as a source of functional compounds—recent developments. *Trends Food Sci Technol* 12(11):401–413
- Kang H, Tang K, Liu Q, Sun Y, Huang Q, Zhu R, Gao J, Zhang D, Huang C, Cao Z (2013) HIM-herbal ingredients in-vivo metabolism database. *J Cheminformatics* 5:28–28. <https://doi.org/10.1186/1758-2946-5-28>
- Release S (2013) 1: Schrödinger Suite 2013 Protein Preparation Wizard. Epik version 2:2013
- Suite S (2013) Protein Preparation Wizard. Schrödinger, LLC, New York
- Release S (2016) 3: LigPrep. Schrödinger, LLC, New York
- Banks JL, Beard HS, Cao Y, Cho AE, Damm W, Farid R, Felts AK, Halgren TA, Mainz DT, Maple JR (2005) Integrated modeling program, applied chemical theory (IMPACT). *J Comput Chem* 26(16): 1752–1780
- Shelley JC, Cholleti A, Frye LL, Greenwood JR, Timlin MR, Uchimaya M (2007) Epik: a software program for pK_a prediction and protonation state generation for drug-like molecules. *J Comput Aided Mol Des* 21(12):681–691
- Dash R, Hosen S, Karim M, Kabir MSH, Hossain MM, Junaid M, Islam A, Paul A, Khan MA (2015) In silico analysis of indole-3-carbinol and its metabolite DIM as EGFR tyrosine kinase inhibitors in platinum resistant ovarian cancer vis a vis ADME/T property analysis. *J Appl Pharm Sci* 5(11):73–78
- Berman HM, Westbrook J, Feng Z, Gilliland G, Bhat TN, Weissig H, Shindyalov IN, Bourne PE (2000) The Protein Data Bank. *Nucleic Acids Res* 28(1):235–242
- Banerjee K, Gupta U, Gupta S, Wadhwa G, Gabrani R, Sharma SK, Jain CK (2011) Molecular docking of glucosamine-6-phosphate synthase in *Rhizopus oryzae*. *Bioinformatics* 7(6):285
- Friesner RA, Banks JL, Murphy RB, Halgren TA, Klicic JJ, Mainz DT, Repasky MP, Knoll EH, Shelley M, Perry JK, Shaw DE, Francis P, Shenkin PS (2004) Glide: a new approach for rapid, accurate docking and scoring. 1 Method and assessment of docking accuracy. *J Med Chem* 47(7):1739–1749
- Friesner RA, Murphy RB, Repasky MP, Frye LL, Greenwood JR, Halgren TA, Sanschagrin PC, Mainz DT (2006) Extra precision glide: docking and scoring incorporating a model of hydrophobic enclosure for protein-ligand complexes. *J Med Chem* 49(21):6177–6196
- Schrödinger L (2012) QikProp, version 3.5. New York
- Natarajan A, Sugumar S, Bitragunta S, Balasubramanian N (2015) Molecular docking studies of (4Z, 12Z)-cyclopentadeca-4, 12-dienone from *Grewia hirsuta* with some targets related to type 2 diabetes. *BMC Complement Altern Med* 15(1):73
- Vijayakumar B, Umamaheswari A, Puratchikody A, Velmurugan D (2011) Selection of an improved HDAC8 inhibitor through structure-based drug design. *Bioinformatics* 7(3):134–141
- Chen F, Liu H, Sun H, Pan P, Li Y, Li D, Hou T (2016) Assessing the performance of the MM/PBSA and MM/GBSA methods. 6. Capability to predict protein–protein binding free energies and re-rank binding poses generated by protein–protein docking. *Phys Chem Chem Phys* 18(32):22129–22139
- Xu L, Sun H, Li Y, Wang J, Hou T (2013) Assessing the performance of MM/PBSA and MM/GBSA methods. 3. The impact of

- force fields and ligand charge models. *J Phys Chem B* 117(28): 8408–8421
33. Sun H, Li Y, Tian S, Xu L, Hou T (2014) Assessing the performance of MM/PBSA and MM/GBSA methods. 4. Accuracies of MM/PBSA and MM/GBSA methodologies evaluated by various simulation protocols using PDBbind data set. *Phys Chem Chem Phys* 16(31):16719–16729
 34. Sun H, Li Y, Shen M, Tian S, Xu L, Pan P, Guan Y, Hou T (2014) Assessing the performance of MM/PBSA and MM/GBSA methods. 5. Improved docking performance using high solute dielectric constant MM/GBSA and MM/PBSA rescoring. *Phys Chem Chem Phys* 16(40):22035–22045
 35. Hou T, Li N, Li Y, Wang W (2012) Characterization of domain–peptide interaction interface: prediction of SH3 domain-mediated protein–protein interaction network in yeast by generic structure-based models. *J Proteome Res* 11(5):2982–2995
 36. Li J, Abel R, Zhu K, Cao Y, Zhao S, Friesner RA (2011) The VSGB 2.0 model: a next generation energy model for high resolution protein structure modeling. *Proteins* 79(10):2794–2812. <https://doi.org/10.1002/prot.23106>
 37. Krieger E, Vriend G, Spronk C (2013) YASARA—Yet Another Scientific Artificial Reality Application. <http://yasara.org/>
 38. Dickson CJ, Madej BD, Skjervek ÅA, Betz RM, Teigen K, Gould IR, Walker RC (2014) Lipid14: the amber lipid force field. *J Chem Theory Comput* 10(2):865–879
 39. Stewart JJ (1990) MOPAC: a semiempirical molecular orbital program. *J Comput Aided Mol Des* 4(1):1–103
 40. Jakalian A, Jack DB, Bayly CI (2002) Fast, efficient generation of high-quality atomic charges. AM1-BCC model: II. Parameterization and validation. *J Comput Chem* 23(16):1623–1641
 41. Wang J, Wolf RM, Caldwell JW, Kollman PA, Case DA (2004) Development and testing of a general amber force field. *J Comput Chem* 25(9):1157–1174
 42. Jorgensen WL, Chandrasekhar J, Madura JD, Impey RW, Klein ML (1983) Comparison of simple potential functions for simulating liquid water. *J Chem Phys* 79(2):926–935
 43. Krieger E, Vriend G (2015) New ways to boost molecular dynamics simulations. *J Comput Chem* 36(13):996–1007
 44. Krieger E, Nielsen JE, Spronk CA, Vriend G (2006) Fast empirical pKa prediction by Ewald summation. *J Mol Graph Model* 25(4): 481–486. <https://doi.org/10.1016/j.jmgl.2006.02.009>
 45. Hess B, Bekker H, Berendsen HJ, Fraaije JG (1997) LINCS: a linear constraint solver for molecular simulations. *J Comput Chem* 18(12):1463–1472
 46. Miyamoto S, Kollman PA (1992) Settle: an analytical version of the SHAKE and RATTLE algorithm for rigid water models. *J Comput Chem* 13(8):952–962
 47. Essmann U, Perera L, Berkowitz ML, Darden T, Lee H, Pedersen LG (1995) A smooth particle mesh Ewald method. *J Chem Phys* 103(19):8577–8593
 48. Berendsen HJ, Jv P, van Gunsteren WF, DiNola A, Haak J (1984) Molecular dynamics with coupling to an external bath. *J Chem Phys* 81(8):3684–3690
 49. Krieger E, Koraimann G, Vriend G (2002) Increasing the precision of comparative models with YASARA NOVA—a self-parameterizing force field. *Proteins* 47(3):393–402
 50. Humphrey W, Dalke A, Schulten K (1996) VMD: visual molecular dynamics. *J Mol Graph* 14(1):33–38
 51. Dash R, Das R, Junaid M, Akash MFC, Islam A, Hosen SZ (2017) In silico-based vaccine design against Ebola virus glycoprotein. *Advances and Applications in Bioinformatics and Chemistry: AABC* 10:11
 52. Mitra S, Dash R (2018) Structural dynamics and quantum mechanical aspects of shikonin derivatives as CREBBP Bromodomain inhibitors. *J Mol Graph Model* 83:42–52
 53. Srinivasan E, Rajasekaran R (2016) Computational investigation of curcumin, a natural polyphenol that inhibits the destabilization and the aggregation of human SOD1 mutant (Ala4Val). *RSC Adv* 6(104):102744–102753
 54. Folkman J (1971) Tumor angiogenesis: therapeutic implications. *N Engl J Med* 285(21):1182–1186. <https://doi.org/10.1056/nejm197111182852108>
 55. Chung AS, Lee J, Ferrara N (2010) Targeting the tumour vasculature: insights from physiological angiogenesis. *Nat Rev Cancer* 10(7):505–514. <https://doi.org/10.1038/nrc2868>
 56. Hoi PM, Li S, Vong CT, Tseng HHL, Kwan YW, Lee SM-Y (2015) Recent advances in structure-based drug design and virtual screening of VEGFR tyrosine kinase inhibitors. *Methods* 71:85–91
 57. Aparna V, Dineshkumar K, Mohanalakshmi N, Velmurugan D, Hopper W (2014) Identification of natural compound inhibitors for multidrug efflux pumps of *Escherichia coli* and *Pseudomonas aeruginosa* using in silico high-throughput virtual screening and in vitro validation. *PLoS One* 9(7):e101840
 58. Jorgensen WL, Duffy EM (2002) Prediction of drug solubility from structure. *Adv Drug Deliv Rev* 54(3):355–366
 59. Jorgensen WL, Duffy EM (2000) Prediction of drug solubility from Monte Carlo simulations. *Bioorg Med Chem Lett* 10(11):1155–1158
 60. Duffy EM, Jorgensen WL (2000) Prediction of properties from simulations: free energies of solvation in hexadecane, octanol, and water. *J Am Chem Soc* 122(12):2878–2888
 61. Cavalli A, Poluzzi E, De Ponti F, Recanatini M (2002) Toward a pharmacophore for drugs inducing the long QT syndrome: insights from a CoMFA study of HERG K+ channel blockers. *J Med Chem* 45(18):3844–3853
 62. De Ponti F, Poluzzi E, Montanaro N (2001) Organising evidence on QT prolongation and occurrence of Torsades de pointes with non-antiarrhythmic drugs: a call for consensus. *Eur J Clin Pharmacol* 57(3):185–209
 63. Vandenberg JI, Walker BD, Campbell TJ (2001) HERG K+ channels: friend and foe. *Trends Pharmacol Sci* 22(5):240–246
 64. Chiesa N, Rosati B, Arcangeli A, Olivetto M, Wanke E (1997) A novel role for HERG K+ channels: spike-frequency adaptation. *J Physiol* 501(2):313–318
 65. Aronov AM (2005) Predictive in silico modeling for hERG channel blockers. *Drug Discov Today* 10(2):149–155
 66. Dash R, Das R, Junaid M, Akash MFC, Islam A, Hosen SMZ (2017) Molecular insight and binding pattern analysis of Shikonin as a potential VEGFR-2 inhibitor. *Curr Enzym Inhib* 13(3):235–244
 67. Huang L, Huang Z, Bai Z, Xie R, Sun L, Lin K (2012) Development and strategies of VEGFR-2/KDR inhibitors. *Future Med Chem* 4(14):1839–1852
 68. Kornev AP, Haste NM, Taylor SS, Ten Eyck LF (2006) Surface comparison of active and inactive protein kinases identifies a conserved activation mechanism. *Proc Natl Acad Sci USA* 103(47): 17783–17788
 69. Bogoyevitch MA, Barr RK, Ketterman AJ (2005) Peptide inhibitors of protein kinases—discovery, characterisation and use. *Biochim Biophys Acta* 1754(1):79–99
 70. Garuti L, Roberti M, Bottegoni G (2010) Non-ATP competitive protein kinase inhibitors. *Curr Med Chem* 17(25):2804–2821
 71. Kamaraj B, Purohit R (2013) In silico screening and molecular dynamics simulation of disease-associated nsSNP in TYR1P1 gene and its structural consequences in OCA3. *BioMed Res Int* 2013: 697051

72. Wang Y, Li Y, Ma Z, Yang W, Ai C (2010) Mechanism of microRNA-target interaction: molecular dynamics simulations and thermodynamics analysis. *PLoS Comput Biol* 6(7):e1000866. <https://doi.org/10.1371/journal.pcbi.1000866>
73. Blatt JM, Weisskopf VF (1991) *Theoretical nuclear physics*. Courier Dover, New York
74. Lovering AL, Lee SS, Kim Y-W, Withers SG, Strynadka NC (2005) Mechanistic and structural analysis of a family 31 α -glycosidase and its glycosyl-enzyme intermediate. *J Biol Chem* 280(3):2105–2115
75. Vieth M, Higgs RE, Robertson DH, Shapiro M, Gragg EA, Hemmerle H (2004) Kinomics—structural biology and chemogenomics of kinase inhibitors and targets. *Biochim Biophys Acta* 1697(1–2):243–257
76. Ghose AK, Herbertz T, Pippin DA, Salvino JM, Mallamo JP (2008) Knowledge based prediction of ligand binding modes and rational inhibitor design for kinase drug discovery. *J Med Chem* 51(17): 5149–5171

Publisher's note Springer Nature remains neutral with regard to jurisdictional claims in published maps and institutional affiliations.